CONNECTING IN SITU STRESS AND WELLBORE DEVIATION TO NEAR-WELL FRACTURE COMPLEXITY USING PHASE-FIELD SIMULATIONS

Organization:	University of Utah
Recipient Organization:	Lawrence Livermore National Laboratory
DUNS Number:	009095365
Recipient Address:	7000 East Ave. Livermore, CA 94550
Award Number:	2-2446
Project Title:	Closing the loop between in situ stress complexity and EGS fracture complexity
Project Period:	10/01/2021 – 06/30/2025
Principal Investigator(s):	Matteo Cusini (PI) cusini1@llnl.gov Andrew Bunger (Co-PI) bunger@pitt.edu
Report prepared by:	Fan Fei (LLNL) Matteo Cusini (LLNL)
Report Submitted by:	Matteo Cusini
Date of Report Submission:	January 30, 2025
Related milestones:	MILESTONE 2.1.1

This work was performed under the auspices of the U.S. Department of Energy by Lawrence Livermore National Laboratory under Contract DE-AC52-07NA27344.

1 Introduction

The interactions among in situ stress, rock fabric, wellbore geometry, natural fractures, and other natural or man-made defects create highly complex fracture trajectories in the near-wellbore region, far more intricate than those in the far-field. These near-wellbore complexities are critical for the Utah FORGE project and Enhanced Geothermal Systems (EGS) in general. Frictional pressure loss in the near-wellbore region during stimulation can significantly influence the growth of far-field fractures, while pressure losses during circulation serve as a major source of energy dissipation.

Near-wellbore fracture complexities are often observable through image logs, offering valuable insights into in situ stress characteristics. However, leveraging this information requires a high-fidelity model capable of capturing the interplay among the diverse factors influencing fracture behavior.

The phase field method (Mikelić et al., 2015; Miehe & Mauthe, 2016; Kumar et al., 2020) presents significant advantages over discrete fracture approaches for modeling the complex geometries of hydraulic fractures in the near-wellbore region. As part of this research project, a novel phase field formulation was developed, enabling the modeling of hydraulic fracture propagation from an initial fracture as well as the nucleation of fractures within the bulk material (Fei et al., 2023). Simultaneously, as part of this research effort, laboratory experiments were conducted to investigate how factors such as stress regimes, wellbore orientation, and thermal cooling influence fracture nucleation patterns.

In this work, the phase field method, as presented in (Fei et al., 2023), is employed to conduct a comprehensive set of numerical experiments aimed at exploring the intricate relationships among near-wellbore fracture nucleation complexity, in situ stress conditions, and wellbore deviation. The model is designed to complement the experimental work performed as part of the project. Accordingly, the numerical experiments are tailored to represent the experimental setup, with rock properties calibrated based on a simple experiment chosen as the base case.

This report is organized as follows: Section 2 provides a brief overview of the phase field formulation and presents the model setup, including geometry, boundary conditions, and the design of numerical experiments. Section 3 discusses the numerical results under varying wellbore inclinations and stress conditions. Finally, Section 4 concludes the report with a summary of key findings and an overview of future work.

2 Phase-field Formulation and Problem Setup

This section provides the details of the phase-field model and the problem setup for this numerical study. More specifically, we first introduce the phase-field approximation of fractures and the formulation employed for modeling near-well hydraulic fracturing. Subsequently, we design a series of numerical experiments to investigate the effects of the in-situ stress condition and wellbore deviation on the near-well fracture pattern.

2.1 Phase-field approximation and governing equations

Let us consider a poroelastic domain Ω fully saturated by a compressible fluid. The domain boundary, $\partial\Omega$, consists of a displacement boundary $\partial_u\Omega$, a traction boundary $\partial_t\Omega$, a pressure boundary $\partial_p\Omega$ and a flux boundary $\partial_q\Omega$, such that

$$\partial_u\Omega \cup \partial_t\Omega = \partial\Omega, \quad \partial_u\Omega \cap \partial_t\Omega = \emptyset, \tag{1}$$

$$\partial_p\Omega \cup \partial_q\Omega = \partial\Omega, \quad \partial_p\Omega \cap \partial_q\Omega = \emptyset. \tag{2}$$

Hydraulic fractures Γ may nucleate and evolve inside the domain. To model hydraulic fracturing, we solve the displacement $\boldsymbol{u}$, the pressure p, and the fracture geometry Γ in the time interval $[0, T]$.

The phase field method approximates hydraulic fractures Γ with a diffusely distributed damage variable $d \in [0, 1]$, where $d = 0$ indicates a fully intact material and $d = 1$ indicates a completely damaged (fractured) material. With this approximation, the strong form equations that govern the evolution of the displacement ($\boldsymbol{u}$), the fluid pressure (p), and the damage field (d) can be written as

$$\nabla \cdot [\boldsymbol{\sigma}'(\boldsymbol{\varepsilon}, d) - m(d)(b-1)p\mathbf{1}] - m(d)\nabla p + \rho\boldsymbol{g} = \mathbf{0}, \tag{3}$$

$$\begin{cases} 2(d-1)W^e - m'(d)bp\nabla\cdot\boldsymbol{u} + m'(d)\nabla\cdot(p\boldsymbol{u}) + \dfrac{3\mathcal{G}_c}{8L}\left[1 - 2L^2\nabla d\right] + c_e = 0, \ d > 0, \\ 2(d-1)W^e - m'(d)bp\nabla\cdot\boldsymbol{u} + m'(d)\nabla\cdot(p\boldsymbol{u}) + \dfrac{3\mathcal{G}_c}{8L}\left[1 - 2L^2\nabla d\right] + c_e \le 0, \ d = 0, \end{cases} \tag{4}$$

$$\frac{\partial}{\partial t}\left(\phi\rho_f\right) + \nabla\cdot\left(\rho_f\boldsymbol{v}\right) = s, \tag{5}$$

subject to the appropriate boundary and initial conditions. Here, Eq. (3) describes the momentum balance equation, where $\boldsymbol{\sigma}'$ is the effective stress tensor, $\boldsymbol{\varepsilon}$ is the strain tensor, $m(d)$ is a damage-dependent function, b is the rock Biot's coefficient, and $\rho\boldsymbol{g}$ is the body force. Eq. (4) is the

damage evolution equation, where $W^e(\boldsymbol{\varepsilon})$ is the strain energy of the intact material, $\mathcal{G}_c$ is the critical fracture energy, L is the phase-field regularization length, and $c_e(\boldsymbol{\sigma}', L)$ is an external driving force term characteristic of the material strength surface, originally introduced in Kumar et al. (2020). Finally, Eq. (5) governs the flow mass balance, in which ϕ is the rock porosity, ρ_f is the fluid density, s is the source/sink term, and $\boldsymbol{v}$ is the Darcy's velocity of the flow, which can be calculated as

$$\boldsymbol{v} = -\frac{\boldsymbol{k}}{\mu_f} \cdot (\boldsymbol{\nabla} p - \rho_f \boldsymbol{g}). \tag{6}$$

Here, $\boldsymbol{k}$ is the permeability tensor, μ_f is the fluid viscosity. To simplify the computation of fracture permeability, we employ an empirical relationship defining permeability as a function of damage (Pijaudier-Cabot et al., 2009).

For additional information including mathematical derivation and model verification, we encourage the readers to refer to our publication (Fei et al., 2023).

2.2 Design of Numerical Experiments

Next, we design a series of numerical tests to systematically investigate the relationship between near-well fracture complexity, in situ stress conditions, and wellbore deviation. These tests are based on the setup of the lab-scale hydraulic fracturing experiment conducted in Task 4. The problem geometry and boundary conditions are illustrated in Fig. 1 for the vertical well (left) and the horizontal well (right), respectively. The domain is a 150 mm × 150 mm × 150 mm granite cube subject to three principal stresses, namely σ_h, σ_H, and σ_v along x, y, and z axis, respectively. A cylindrical well with the diameter of 12.8 mm is drilled through the center of the domain. For the vertical well, the well is along the direction of σ_v, while for the horizonal well, the well is along the direction of σ_h. The pressurization on the wellbore due to fluid injection is only applied in the middle shaded section by prescribing a pressure boundary condition $\hat{p}_{\text{inj}}(t)$.

In this work, we study the impact of well deviation on near-well hydraulic fracturing in two aspects: (i) the axis/axes about which the wellbore is rotated, and (ii) the deviation angle θ. For the rotational axes, three cases are considered: rotation of the wellbore about either of the stress axes traversing the wellbore, or rotation about both axes following the right-hand rule. For the vertical well, this involves counterclockwise rotation of the wellbore about the σ_h (y) axis, the σ_H (x) axis, or both axes. For the horizontal well, the wellbore is rotated counterclockwise about the σ_v (z) axis, the σ_H (x) axis, or both axes. For each rotation scenario, simulations are performed at two angles, $\theta = 10^\circ$ and $\theta = 15^\circ$. Additionally, a benchmark case with no wellbore deviation is modeled as a reference.

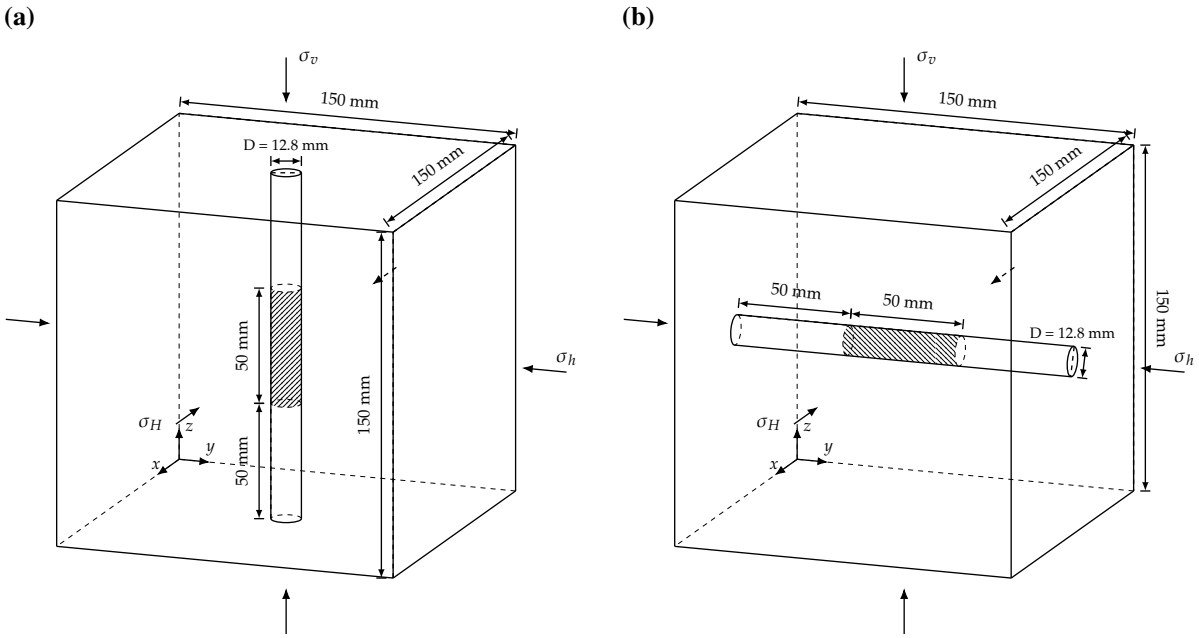

Figure 1: Problem geometry and boundary conditions for (a) the vertical well and (b) the horizontal well.

Stress regime	Stress orientation ($\sigma_{\text{max}} - \sigma_{\text{int}} - \sigma_{\text{min}}$)
Normal	$\sigma_v - \sigma_H - \sigma_h$
Reverse	$\sigma_H - \sigma_h - \sigma_v$
Strike-slip	$\sigma_H - \sigma_v - \sigma_h$

Table 1: Scenarios with different stress orientations according to Anderson's faulting theory.

Regarding the in situ stress condition, we investigate the effects of two independent factors: (i) the stress orientation with respect to the well, and (ii) the magnitude of the minimum principal stress. To study the effects of the stress orientation, we follow Anderson's faulting theory and consider three scenarios as presented in Table 1 for both vertical and horizontal wells, where σ_{max}, σ_{int}, σ_{min} denote the maximum, intermediate, and minimum principal stress, respectively. For each stress orientation, we also study the effects of the stress magnitude by adopting three different values of σ_{min}, namely 3 MPa, 7 MPa, and 10 MPa, while fixing σ_{max} = 17.5 MPa and σ_{int} = 15 MPa.

Table 2 summarizes the details of each parameter studied in this numerical experiment for both vertical and horizontal wells. In total, 63 cases are simulated for each well orientation.

Well orientation	In situ stress condition		Wellbore deviation	
	$\sigma_{\min}$ magnitude (MPa)	Stress orientation	Rotational axis	Deviation angle θ
Vertical	3, 7, 10	Normal Reverse Strike-slip	σ_h, σ_H, both σ_h & σ_H	No deviation, 10°, 15°
Horizontal	3, 7, 10	Normal Reverse Strike-slip	σ_H, σ_v, both σ_H & σ_v	No deviation, 10°, 15°

Table 2: Summary of all cases for the numerical experiment.

2.3 Assumptions & limitations

It is important to point out the following assumptions and limitations of this modeling study.

- This study is restricted to hydraulically induced fractures, meaning the conclusions may not directly apply to other types of fractures or damage, such as drill-induced fractures or borehole breakouts. However, the phase-field formulation employed in this work is not limited to hydraulic fracturing and could be extended to other failure mechanisms. Systematic studies are required to explore different types of near-well failures for stress characterization.

- In this study, the width of the injection zone is fixed at one-third of the domain height. In real-world injection scenarios, the perforation zone is typically much smaller relative to the reservoir scale. Consequently, potential boundary effects may influence both experimental and numerical results. Future research should investigate the impact of varying injection zone sizes on near-wellbore fracture patterns.

- A Drucker-Prager yield criterion is employed to identify fracture nucleation. The validity of the results is inherently affected by this choice and depends on the assumption that this criterion is appropriate for granitic rocks. Further work is necessary to assess the sensitivity of the results to alternative yield criteria.

3 Numerical experiments

In this section, we present the simulation results for all cases summarized in Table 2. The discussion begins with the benchmark case, which is used to calibrate the phase-field model parameters based on experimental results. The calibrated parameters are then applied to all

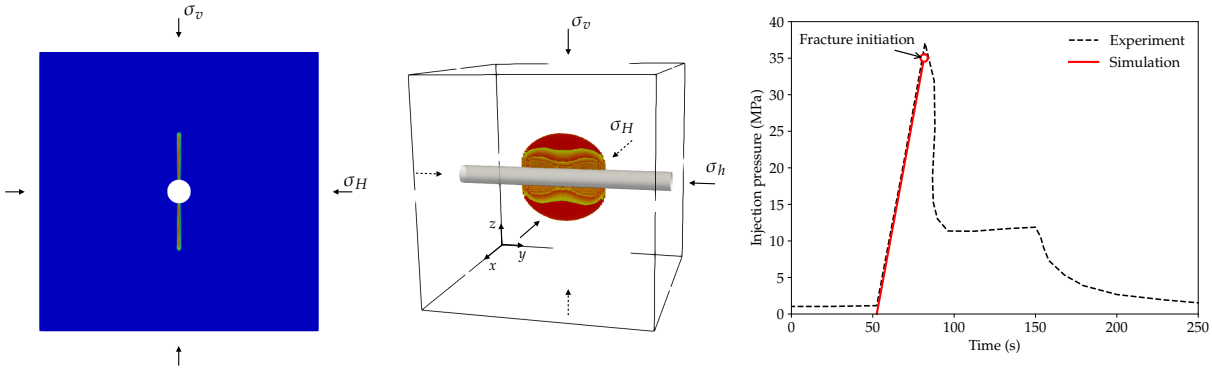

Figure 2: Simulation results of the benchmark example

simulation cases, and their results are later processed and categorized based on the near-well fracture pattern obtained.

3.1 Benchmark case & model calibration

To begin, the material parameters for the phase-field model are determined by calibrating against the fracture initiation pressure obtained from a laboratory test conducted for a benchmark example. This benchmark example involves a horizontal well subjected to a normal stress condition, where $\sigma_v > \sigma_H > \sigma_h$, with $\sigma_v = 17.5, \text{MPa}$, $\sigma_H = 10, \text{MPa}$, and $\sigma_h = 3, \text{MPa}$.

Figure 2 presents the simulation results for the benchmark case using the parameters listed in Table 3. As shown in the figure, the simulated fracture initiation pressure aligns closely with the laboratory data. To achieve this match, the critical fracture energy, $\mathcal{G}_c$, and the tensile strength, σ_{ts}, were primarily calibrated, while other parameters were set based on their reference values from the literature (Lu, 2017; Yu et al., 2014). Notably, the calibrated values of $\mathcal{G}_c$ and σ_{ts} fall within the appropriate ranges for granite, ensuring consistency with established material properties.

3.2 Summary of simulation results

With the calibrated parameters from Table 3, we proceed to the main part of this numerical study that is to simulate the near-well hydraulic fracture under varying stress conditions and well deviations. We analyze the simulation results by examining the individual impact of the well deviation and the stress condition. To elucidate their effects on the near-well fracturing behavior, we primarily focus on three key features of the nucleated fractures: (i) the fracture geometry (planar or curved), (ii) the fracture alignment relative to the well (longitudinal or inclined), and (iii) the fracture nucleation location on the well circumference. These features are emphasized

Parameter	Unit	Value
Young's modulus, E	GPa	40
Poisson's ratio, ν	-	0.23
Critical fracture energy, $\mathcal{G}_c$	J/m^2	12
Tensile strength, σ_{ts}	MPa	18
Compressive strength, σ_{cs}	MPa	150
Regularization length, L	mm	1
Grain bulk modulus, K_s	GPa	128.5
Reference porosity, ϕ_0	-	0.05
Fluid viscosity, μ_f	Pa·s	0.001
Fluid density, ρ_f	kg/m^3	1000
Permeability of the intact rock, k_0	Darcy	10^{-6}

Table 3: Parameters for the numerical experiment

because they can be extracted from image log data, allowing us to directly apply the insights gained from these simulations to the field study.

3.2.1 Wellbore deviation

First, we study how the wellbore deviation affects the near-well hydraulic fracture pattern. In the following paragraphs, we present and analyze the results separately for the vertical and horizontal wells.

Vertical well Figures 3-5 summarize all simulation results with different wellbore deviations, focusing on the fracture alignment and geometry. As for the fracture alignment, the middle column provides the angle between the fracture orientation and the wellbore axis to quantitatively show the degree of fracture inclination. We define the fracture to be *Longitudinal* to the well if the angle is below 1°, and *Inclined* if the angle is above 2°. Otherwise, the fracture alignment is considered as an intermediate *Mixed* state. For better illustration, Figures 6 and 7 show the extracted phase-field fractures and the overcored view, respectively, for a representative group of examples under the reverse stress condition with $\sigma_v = \sigma_{\text{min}} = 3$ MPa.

As shown in Figures 3–5, cases with no well deviation consistently exhibit planar hydraulic fractures that are longitudinal to the well, regardless of the stress orientation or magnitude. A similar observation applies to cases where the wellbore is rotated about σ_h: near-well fractures remain planar and longitudinal to the well, independent of the stress condition or deviation angle. In fact, for a vertical well, the near-well hydraulic fracture tends to grow perpendicular to σ_h. When the wellbore is rotated about σ_h, the angle between the wellbore and σ_h remains at 90°,

just as in the benchmark case. As a result, the fracture has no tendency to incline or curve, continuing to propagate perpendicular to σ_h.

However, when the wellbore is rotated about σ_H or both horizontal stress axes, the resulting fracture becomes curved, forming an S-shape, and inclines relative to the wellbore axis, as shown in Figures 6 and 7. Generally, the degree of fracture inclination increases with the wellbore deviation angle, regardless of the orientation or magnitude of the stress field. The curvature of the fracture increases with the wellbore deviation angle, particularly for certain stress orientations. For instance, under normal stress conditions, the fracture transitions from a planar or nearly planar shape to a more pronounced curved configuration as the deviation angle increases. Generally, the degree of fracture inclination increases with the deviation angle, regardless of the orientation or magnitude of the stress field. Regarding the effects of the rotational axis or axes, it is observed that fractures become more curved when the wellbore is rotated about both σ_h and σ_H axes compared to cases where it is rotated about only one axis. This outcome is expected, as rotation about both horizontal stress axes is likely to cause greater alterations to the near-well stress conditions, leading to more irregular fracture geometries. However, no clear relationship is observed between the wellbore rotational axis and the degree of fracture inclination.

In addition to its effects on the fracture shape and its orientation, the well deviation also influences the fracture nucleation location. Figure 8 shows the location of fracture nucleation on the well circumference for a specific set of examples under the reverse stress condition with $\sigma_v = \sigma_{\text{min}} = 3$ MPa. For cases with no well deviation or rotation about either horizontal stress axis, fractures nucleate at the “north” and “south” poles of the circular well, where tensile stress typically concentrates. However, when the wellbore is rotated about both σ_h and σ_H axes, the fracture nucleation location shifts counterclockwise due to altered stress distribution in the near-well region. To quantitatively study this effect, we introduce the fracture azimuth, which is defined as the angle measured counterclockwise from the "north" pole on the circular well. For example, the cases with no well deviation in Figure 8 have 0° in azimuth, while the case with a 10° rotation about both stress axes has a fracture azimuth of 12°. Tables 4-6 summarize the fracture azimuths for all simulation tests. It can be observed that, across all stress orientations and magnitudes, only the cases with well rotation about both stress axes exhibit a nonzero fracture azimuth. This observation aligns with the analytical solution presented in Zoback (2010), where the fracture position consistently occurs near the wellbore wall closest to σ_H, regardless of the vertical well’s deviation about either horizontal stress axis. However, when the well is deviated about both horizontal axes, the fracture position begins to shift. See Figure 8.5 in Zoback (2010) for example. The tables also highlight the effects of the stress orientation and magnitude on the

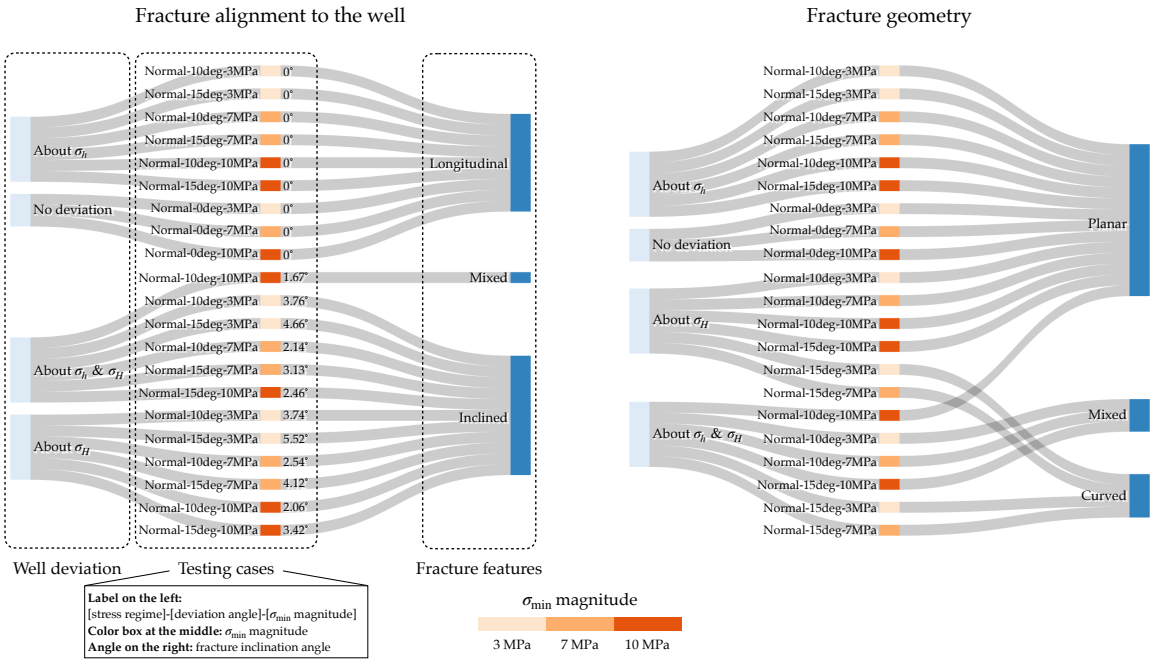

Figure 3: Vertical well: summary of simulation results for different well deviations under the normal stress condition, focusing on the fracture alignment (left) and geometry (right). The left column shows the wellbore deviation axis/axes. The middle column consists of the case label, a color box indicating σ_{min} magnitude, and the fracture inclination angle if applicable. The right column shows the fracture feature, where "Mixed" indicates an intermediate state.

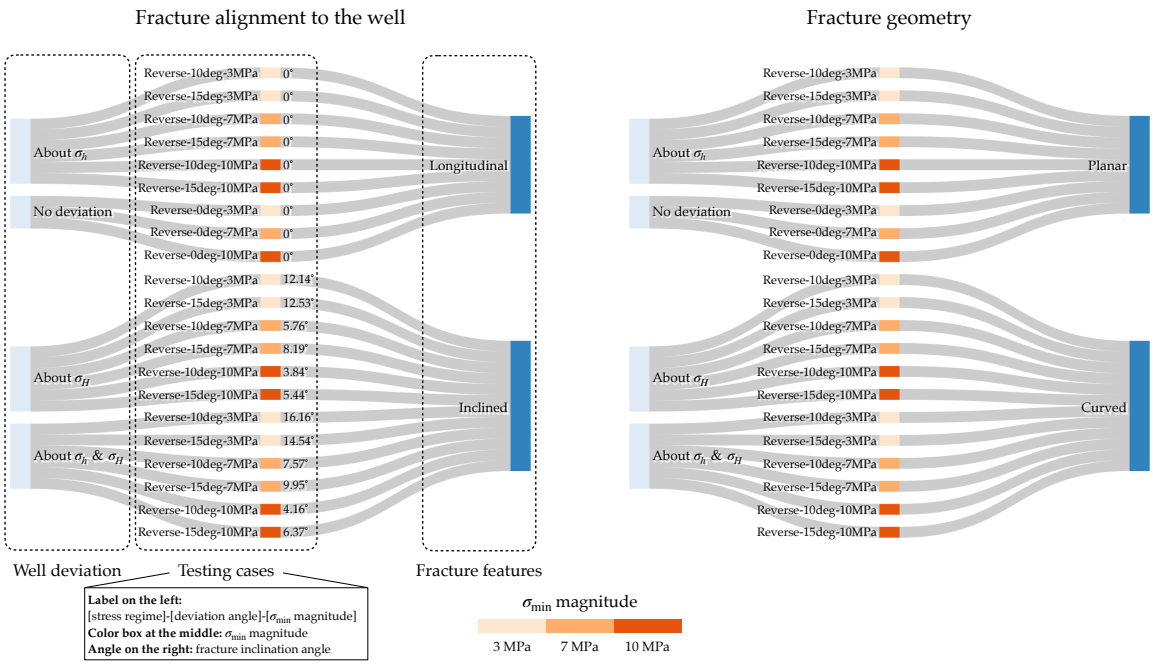

Figure 4: Vertical well: summary of simulation results for different well deviations under the reverse stress condition, focusing on the fracture alignment (left) and geometry (right). The left column shows the wellbore deviation axis/axes. The middle column consists of the case label, a color box indicating σ_{min} magnitude, and the fracture inclination angle if applicable. The right column shows the fracture feature, where "Mixed" indicates an intermediate state.

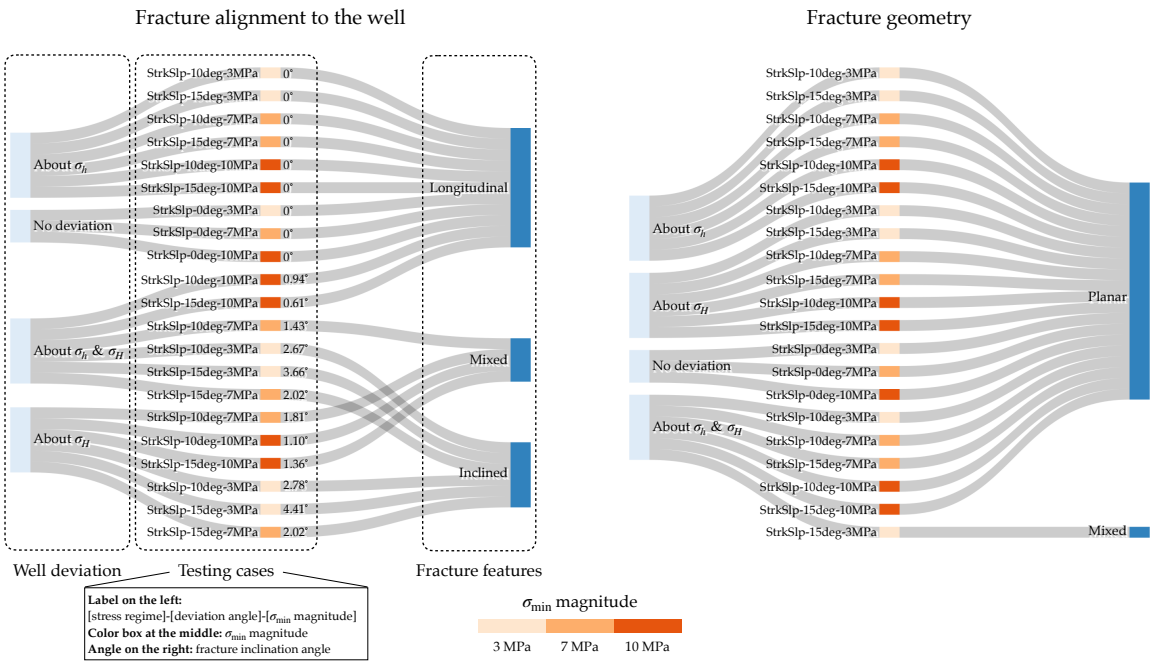

Figure 5: Vertical well: summary of simulation results for different well deviations under the strike slip condition, focusing on the fracture alignment (left) and geometry (right). The left column shows the wellbore deviation axis/axes. The middle column consists of the case label, a color box indicating σ_{min} magnitude, and the fracture inclination angle if applicable. The right column shows the fracture feature, where "Mixed" indicates an intermediate state.

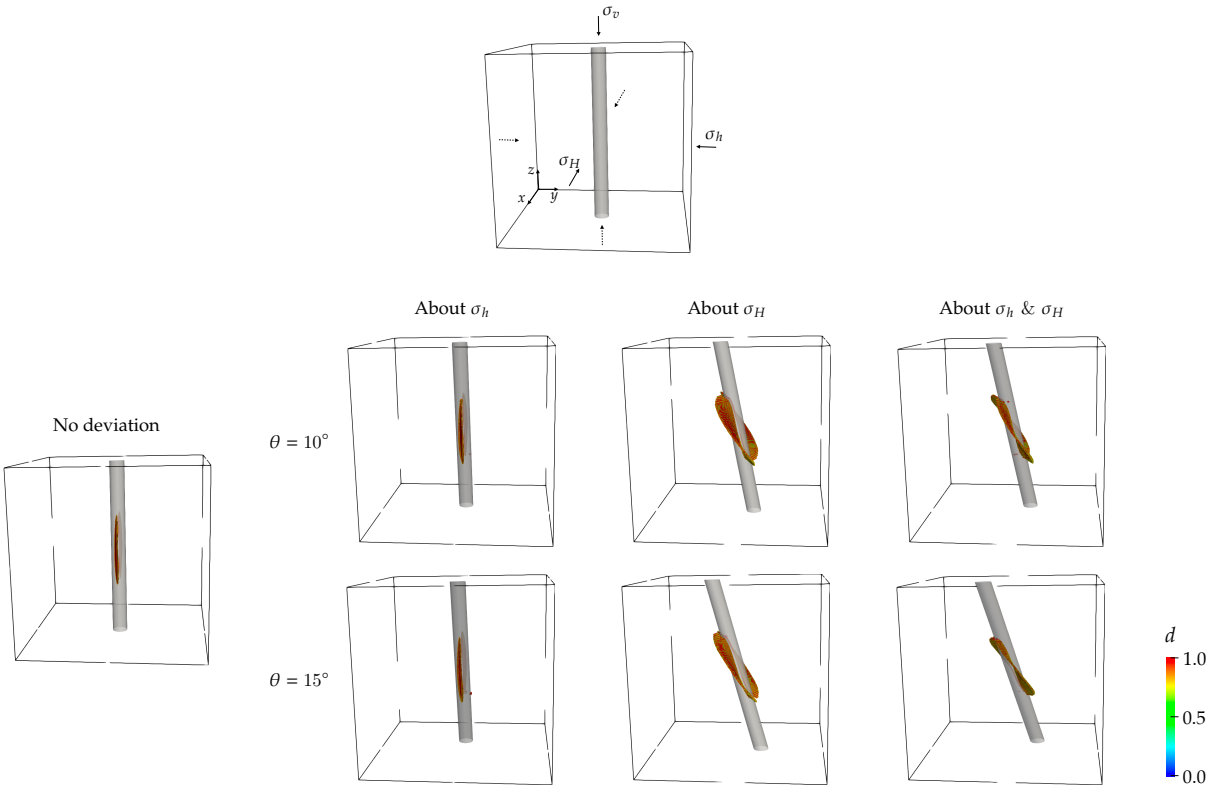

Figure 6: Vertical well: extracted phase-field fractures of representative examples under varying well deviations.

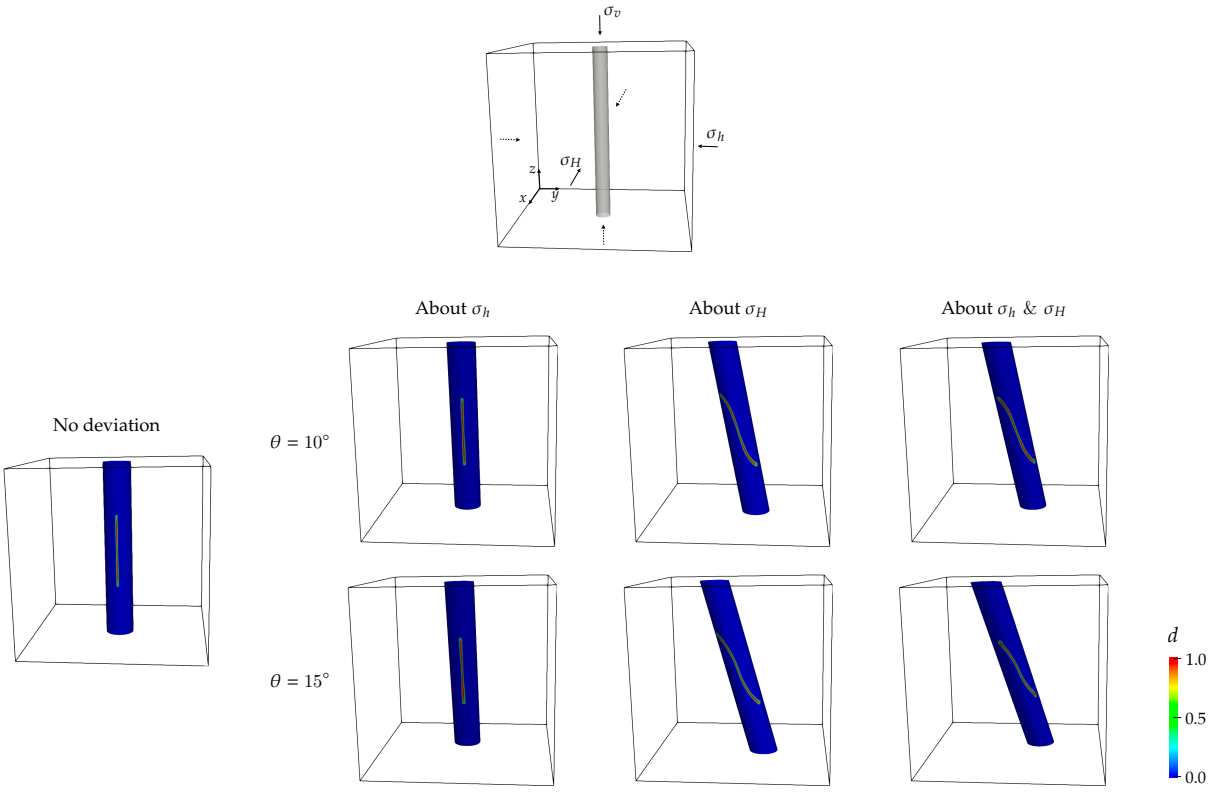

Figure 7: Vertical well: overcored view of representative examples under varying well deviations.

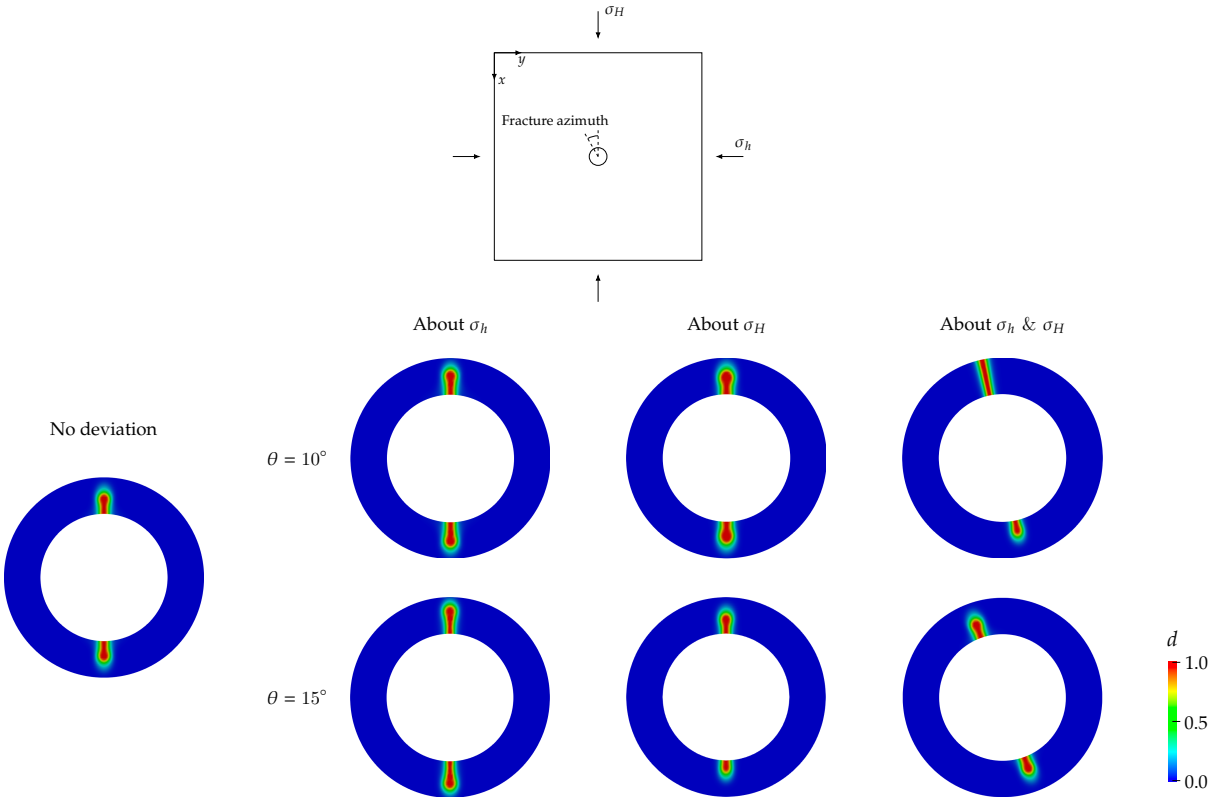

Figure 8: Vertical well: fracture nucleation position on the well circumference for representative examples for different well deviation angles under the reverse stress condition with $\sigma_v = \sigma_{\text{min}} = 3$ MPa.

fracture azimuth, with further details to be discussed later.

Horizontal well Following the approach for the vertical well, Figures 9-11 summarize the simulation results for the horizontal well with varying wellbore deviations under the normal, reverse, and strike-slip stress conditions, respectively. As with the vertical well, examples with no deviation consistently show planar, longitudinal fractures, regardless of stress orientation or magnitude. When the wellbore begins to deviate, however, the near-well fracture may exhibit a curved *S*-shape and incline relative to the well axis, depending on the specific stress regime. For example, as illustrated in Figure 9, under the normal stress condition, the fracture is curved and inclined when the wellbore is rotated about either σ_v or both σ_v and σ_H axes. In contrast, it remains planar and longitudinal when the well rotation is only about σ_H. Things get opposite under the strike-slip condition as presented in Figure 11: the near-well fracture features in a curved shape and inclined alignment when the wellbore is rotated about σ_H only or both stress axes, while maintains a planar shape and longitudinal alignment to the well with rotation only about σ_v. In the reverse stress regime, as displayed in Figure 10, almost all results show planar

Wellbore deviation	Fracture azimuth under the normal stress regime		
	$\sigma_{\min}$ = 3 MPa	$\sigma_{\min}$ = 7 MPa	$\sigma_{\min}$ = 10 MPa
No deviation	0°	0°	0°
About σ_h by 10°	0°	0°	0°
About σ_h by 15°	0°	0°	0°
About σ_H by 10°	0°	0°	0°
About σ_H by 15°	0°	0°	0°
About σ_h & σ_H by 10°	2°	2°	2.5°
About σ_h & σ_H by 15°	1°	1°	1.5°

Table 4: Vertical well: fracture azimuth angles under the normal stress regime.

Wellbore deviation	Fracture azimuth under the reverse stress regime		
	$\sigma_{\min}$ = 3 MPa	$\sigma_{\min}$ = 7 MPa	$\sigma_{\min}$ = 10 MPa
No deviation	0°	0°	0°
About σ_h by 10°	0°	0°	0°
About σ_h by 15°	0°	0°	0°
About σ_H by 10°	0°	0°	0°
About σ_H by 15°	0°	0°	0°
About σ_h & σ_H by 10°	12°	8°	6°
About σ_h & σ_H by 15°	20°	14°	9.5°

Table 5: Vertical well: fracture azimuth angles under the reverse stress regime.

Wellbore deviation	Fracture azimuth under the strike-slip stress regime		
	$\sigma_{\min}$ = 3 MPa	$\sigma_{\min}$ = 7 MPa	$\sigma_{\min}$ = 10 MPa
No deviation	0°	0°	0°
About σ_h by 10°	0°	0°	0°
About σ_h by 15°	0°	0°	0°
About σ_H by 10°	0°	0°	0°
About σ_H by 15°	0°	0°	0°
About σ_h & σ_H by 10°	1.5°	1°	1°
About σ_h & σ_H by 15°	−1°	−1°	−2°

Table 6: Vertical well: fracture azimuth angles under the strike-slip stress regime.

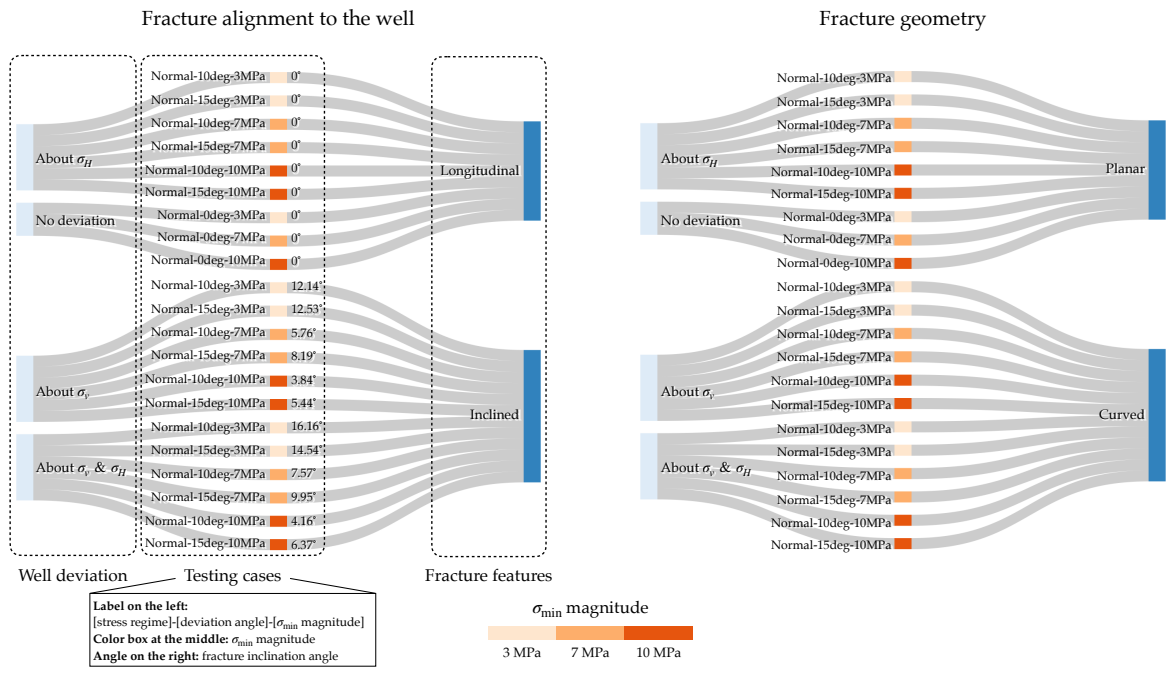

Figure 9: Horizontal well: summary of simulation results for different well deviations under the normal stress condition, focusing on the fracture alignment (left) and geometry (right). The left column shows the wellbore deviation axis/axes. The middle column consists of the case label, a color box indicating σ_{min} magnitude, and the fracture inclination angle if applicable. The right column shows the fracture feature, where "Mixed" indicates an intermediate state.

fractures, irrespective of the rotation axis/axes. Besides, the near-well fracture under the reverse stress condition shows no inclination at all when the well is rotated about only the σ_v axis. Even when the fracture becomes inclined with rotation along other axes, the inclination angle is significantly smaller compared to the normal and strike-slip stress cases. All these observations highlight that the effects of wellbore deviation are clearly dependent on the stress regime the horizontal well is subject to. Also notably, across all three stress regimes, we notice that the fracture inclination generally increases with the deviation angle, suggesting that the stress state near the well gets more altered as the deviation angle grows.

In addition, we provide the fracture nucleation azimuths for all horizontal well cases, with the azimuth angle now defined in the x-z plane, as illustrated in Figure 12. Tables 7-9 individually present the azimuth angles for the normal, reverse, and strike-slip regimes with varying wellbore deviations. Since the effects of wellbore deviation are closely associated with the stress orientation in horizontal wells, we discuss the variation of fracture azimuth with wellbore deviation based on the stress regime. First, we examine the fracture azimuths in Table 7 for the normal stress condition.

As observed, the fracture nucleation point begins to shift counterclockwise from a zero

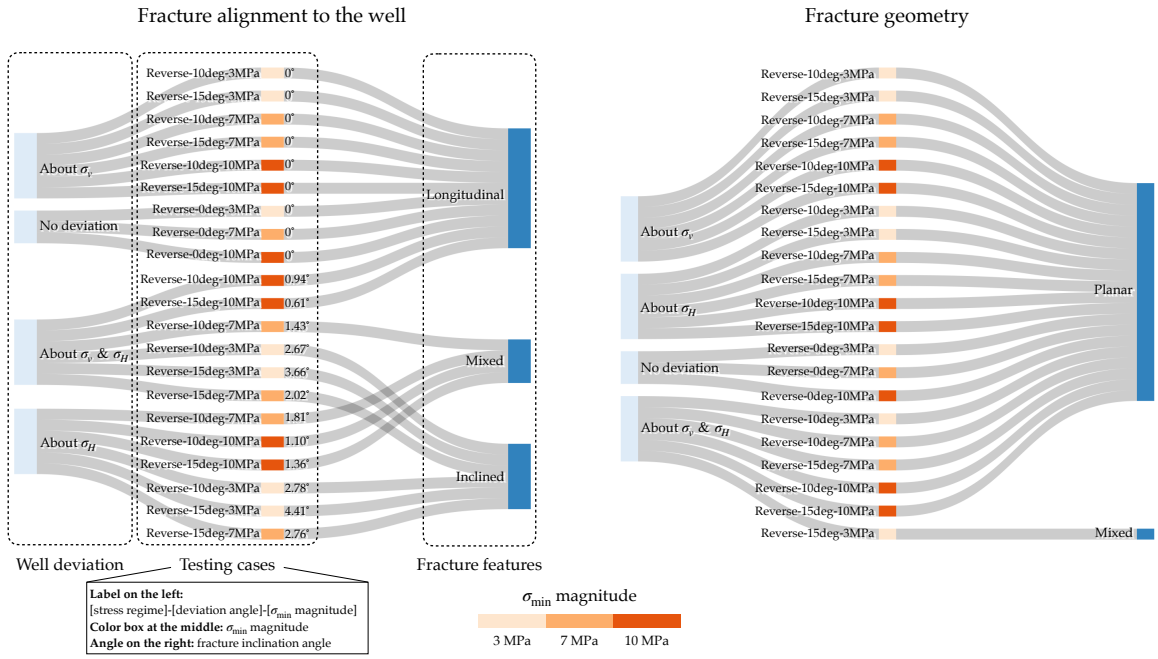

Figure 10: Horizontal well: summary of simulation results for different well deviations under the reverse stress condition, focusing on the fracture alignment (left) and geometry (right). The left column shows the wellbore deviation axis/axes. The middle column consists of the case label, a color box indicating σ_{min} magnitude, and the fracture inclination angle if applicable. The right column shows the fracture feature, where "Mixed" indicates an intermediate state.

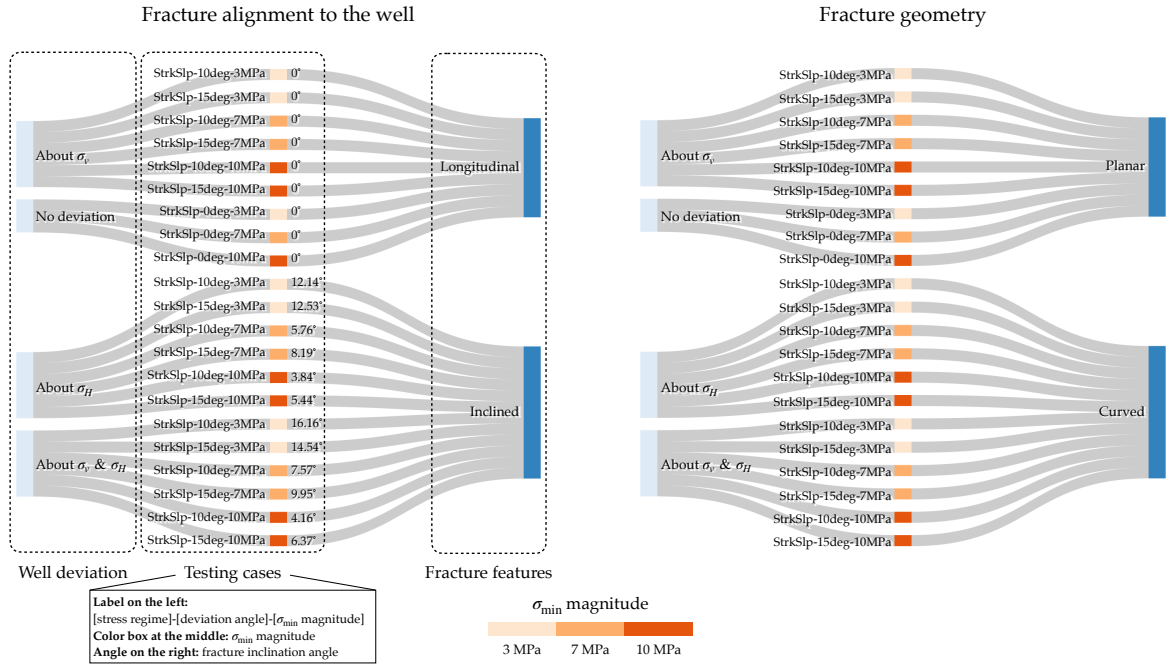

Figure 11: Horizontal well: summary of simulation results for different well deviations under the strike slip condition, focusing on the fracture alignment (left) and geometry (right). The left column shows the wellbore deviation axis/axes. The middle column consists of the case label, a color box indicating σ_{min} magnitude, and the fracture inclination angle if applicable. The right column shows the fracture feature, where "Mixed" indicates an intermediate state.

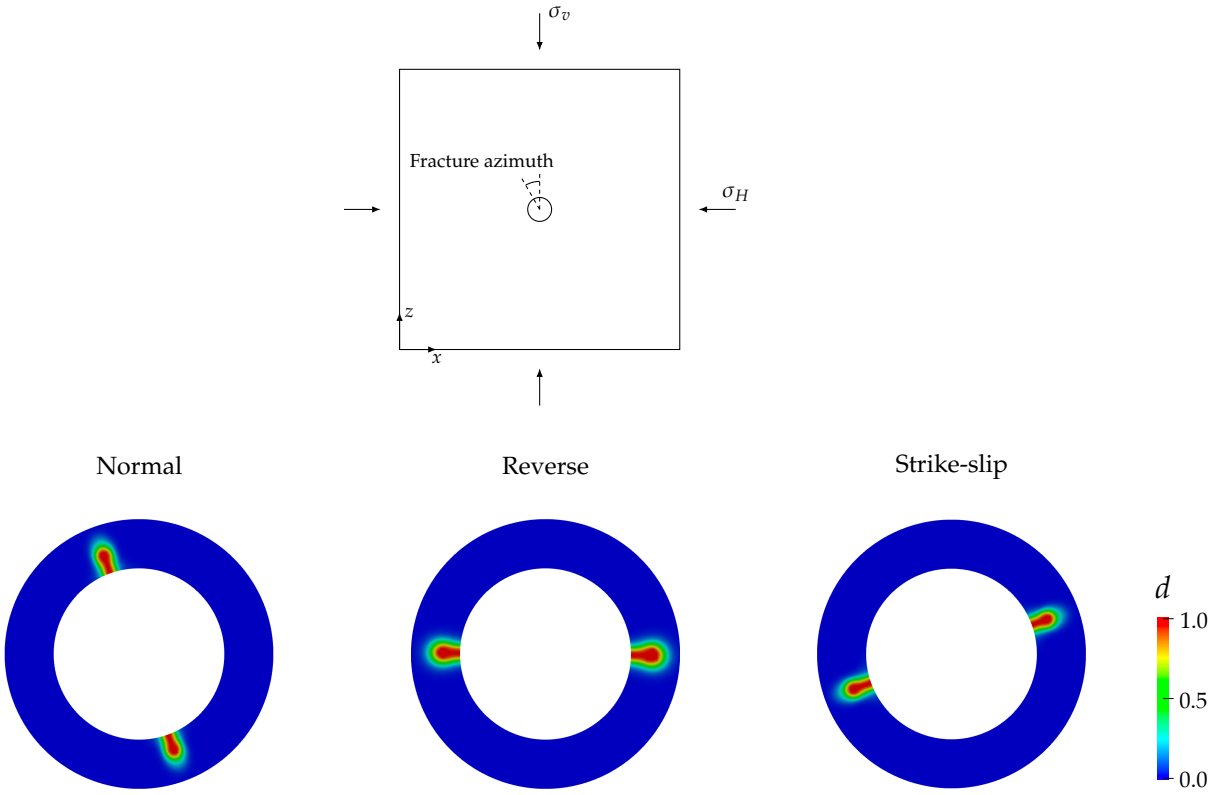

Figure 12: Horizontal well: fracture nucleation position on the well circumference for representative examples in varying stress regimes.

azimuth only when the well is rotated about both σ_v and σ_H axes, resembling the behavior seen in the vertical well cases. Furthermore, the azimuth deviates further from 0° as the wellbore deviation increases, likely due to the greater influence of the local stress state at larger deviation angles.

In contrast to the normal stress case, the fracture nucleation location shifts toward the "west" and "east" poles of the well circle when the stress regime transitions to reverse and strike-slip conditions, respectively, as illustrated in Figure 12. This is because, in the x-z (σ_H-σ_v) plane that traverses the wellbore, σ_H is larger than σ_v under the reverse and strike-slip conditions, whereas it is opposite in the normal stress condition. As a result, the near-well fractures are more normal to the σ_v direction, causing the fracture azimuths shown in Tables 8 & 9 to be closer to 90°. However, a similar trend can be observed in the reverse and strike-slip regimes: the fracture nucleation azimuth only gets deviated when the wellbore rotation is about both the σ_v and σ_H axes.

Wellbore deviation	Fracture azimuth under the normal stress regime		
	$\sigma_{\min}$ = 3 MPa	$\sigma_{\min}$ = 7 MPa	$\sigma_{\min}$ = 10 MPa
No deviation	0°	0°	0°
About σ_v by 10°	0°	0°	0°
About σ_v by 15°	0°	0°	0°
About σ_H by 10°	0°	0°	0°
About σ_H by 15°	0°	0°	0°
About σ_v & σ_H by 10°	12°	8°	6°
About σ_v & σ_H by 15°	20°	14°	9.5°

Table 7: Horizontal well: fracture azimuth angles under the normal stress regime.

Wellbore deviation	Fracture azimuth under the reverse stress regime		
	$\sigma_{\min}$ = 3 MPa	$\sigma_{\min}$ = 7 MPa	$\sigma_{\min}$ = 10 MPa
No deviation	90°	90°	90°
About σ_v by 10°	90°	90°	90°
About σ_v by 15°	90°	90°	90°
About σ_H by 10°	90°	90°	90°
About σ_H by 15°	90°	90°	90°
About σ_v & σ_H by 10°	91.5°	91°	91°
About σ_v & σ_H by 15°	89°	89°	88°

Table 8: Horizontal well: fracture azimuth angles under the reverse stress regime.

Wellbore deviation	Fracture azimuth under the strike-slip stress regime		
	$\sigma_{\min}$ = 3 MPa	$\sigma_{\min}$ = 7 MPa	$\sigma_{\min}$ = 10 MPa
No deviation	90°	90°	90°
About σ_v by 10°	90°	90°	90°
About σ_v by 15°	90°	90°	90°
About σ_H by 10°	90°	90°	90°
About σ_H by 15°	90°	90°	90°
About σ_v & σ_H by 10°	102°	98°	96°
About σ_v & σ_H by 15°	110°	104°	99.5°

Table 9: Horizontal well: fracture azimuth angles under the strike-slip stress regime.

3.2.2 Stress condition

Next, we examine the effects of in situ stress condition on the near-well fracture pattern with a primary focus on the stress orientation and magnitude. Also, we discuss the results separately for vertical and horizontal wells.

Vertical well To better identify the effects of the stress condition, we re-organize the results and present them in Figures 13 & 14, grouping the cases by their respective stress orientations and magnitudes. For brevity, we show only the cases in which the wellbore is rotated about σ_H (Figure 13) or both horizontal stress axes (Figure 14, as other cases all exhibit regular near-well fracture patterns, *i.e.,* planar and longitudinal to the well.

At first, we assess the effects of the stress orientation. As indicated in Figures 13 & 14, for the same stress magnitude, fracture inclination is maximized under reverse stress conditions, while it is minimized under strike-slip conditions. The same trend can be observed for the fracture curvature: fractures are predominantly curved under the reverse stress condition, while they become more planar as the stress orientation changes to the normal regime, ultimately becoming mostly planar under the strike-slip regime. Figure 15 illustrate these observations through a representative group of cases in which the well is rotated about both σ_h and σ_H by 15° and σ_{min} = 3 MPa. This is because, for a vertical well, near-well fracture nucleation and propagation are primarily influenced by the two horizontal stresses. In the strike-slip case, the difference in magnitude between σ_H and σ_h is maximized, resulting in high tensile stress around the well circumference. Consequently, fracture propagation is more likely controlled by the direction of the stress, leading to a more regular fracture pattern with a planar shape. In contrast, when the stress orientation is in a reverse regime, the two horizontal stresses have minimal differences in magnitude, making fracture propagation less likely to be controlled by the stress direction. Additionally, σ_v is at its minimum in the reverse case, providing less vertical compression to the fracture. As a result, the fracture may curve and become more transverse to the well. Also, as we can see across Tables 4-6, the stress orientation influences the azimuth of the fracture nucleation location when the wellbore is rotated about both horizontal stress axes. For the vertical well, the azimuth deviates the most from 0° under the reverse stress condition, where the near-well stress state is altered most due to well deviation. As the stress regime transitions to normal and strike-slip conditions, the azimuth decreases and approaches 0°, indicating that fracture nucleation becomes increasingly governed by the in situ stress conditions. In conclusion, all the observation suggests that for a vertical well, the fracture nucleation and propagation patterns are minimally governed by the in situ stress in a reverse stress regime, while they are predominantly controlled by the in situ stress in a strike-slip regime.

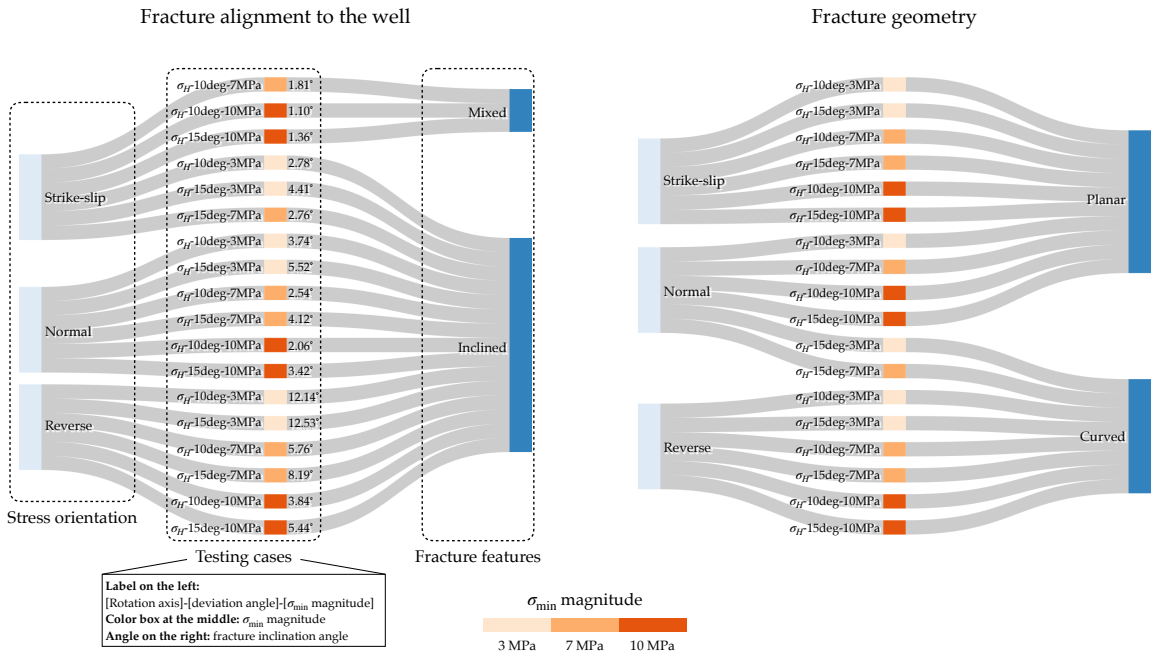

Figure 13: Vertical well: summary of simulation results for different stress conditions with well rotation about σ_H axis, focusing on the fracture alignment (left) and geometry (right). The left column shows the stress regime. The middle column consists of the case label, a color box indicating σ_{min} magnitude, and the fracture inclination angle if applicable. The right column shows the fracture feature, where "Mixed" indicates an intermediate state.

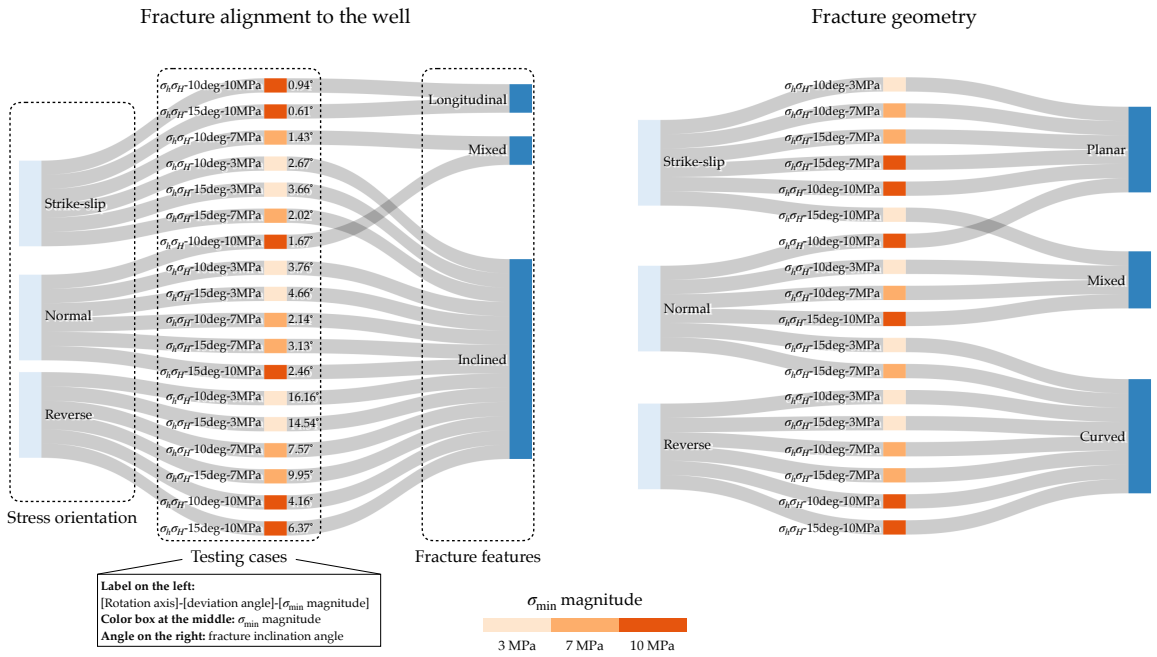

Figure 14: Vertical well: summary of simulation results for different stress conditions with well rotation about both σ_h & σ_H axes, focusing on the fracture alignment (left) and geometry (right). The left column shows the stress regime. The middle column consists of the case label, a color box indicating σ_{min} magnitude, and the fracture inclination angle if applicable. The right column shows the fracture feature, where "Mixed" indicates an intermediate state.

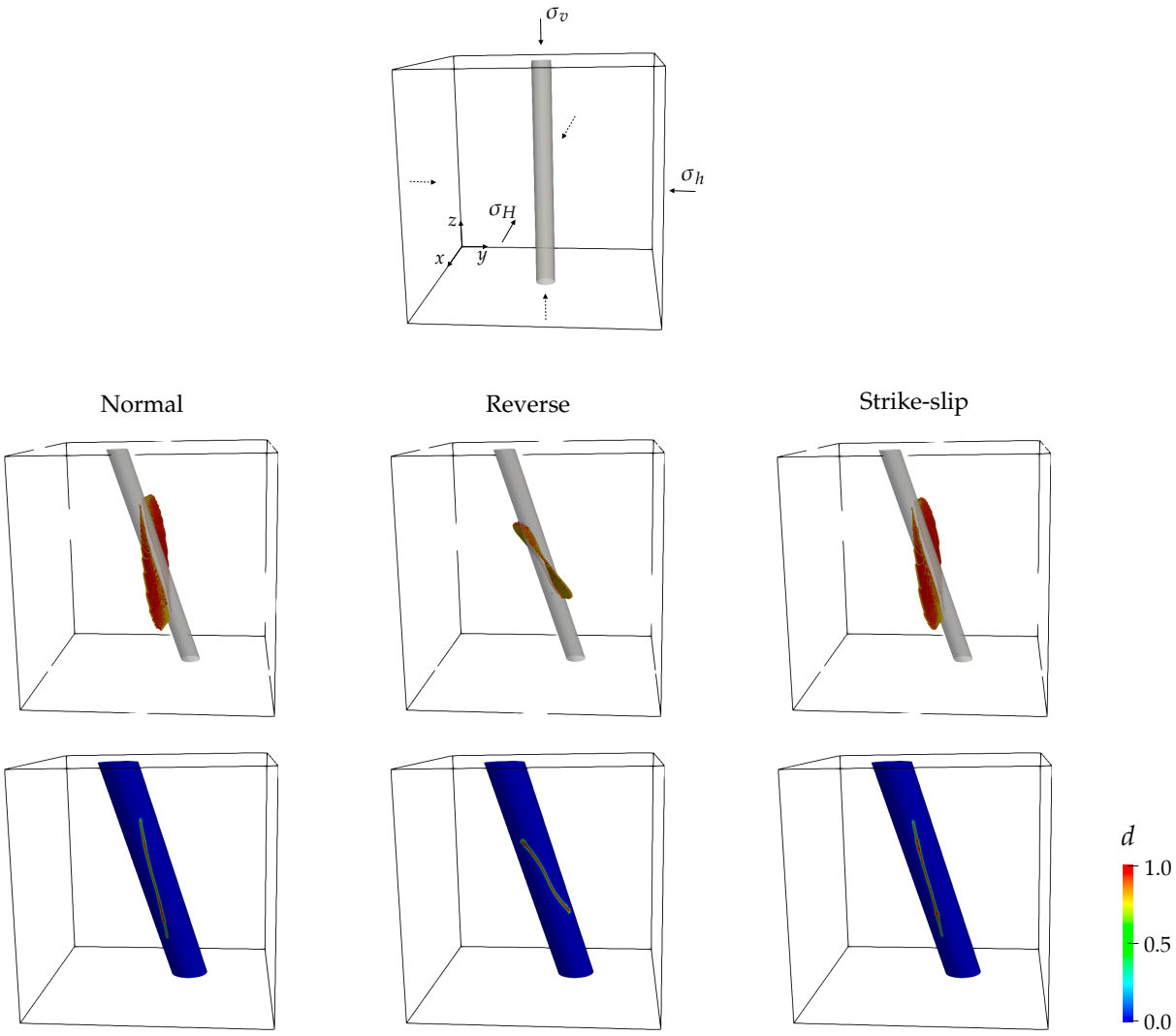

Figure 15: Vertical well: near-well fracture results for representative examples under varying stress orientations.

Next, we analyze the impact of the stress magnitude. As shown in Figures 13 & 14, irrespective of the stress orientation or the wellbore deviation angle, a higher magnitude of $\sigma_{\min}$ leads to near-well fractures that are more planar and longitudinal to the well. Representative examples are displayed in Figure 16, where the well is rotated both about σ_h and σ_H by 10° and a reverse stress is applied. This observation indicates that near-well hydraulic fracturing processes are more dictated by the in situ stress when the stress magnitude is higher. The same conclusion can be drawn from the fracture azimuth results. Except for the normal stress condition, the azimuth decreases with an increasing stress magnitude in the other two stress regimes, as shown in Tables 5 and 6, indicating a more stress-controlled behavior. The different trend observed in the normal stress case is likely due to the excessively small stress difference between σ_H and σ_h when $\sigma_{\min}$ (σ_h) increases, which counteracts the effects of the stress magnitude. Therefore, to study the behavior of near-well fractures in greater detail, we need to consider the interplay between the stress orientation and the ratio of the principal stresses.

Horizontal well Likewise, we re-organize the results for all horizontal well cases based on their stress conditions and present them in Figures 17-19 for each wellbore deviation scenario. We begin by analyzing the effect of the stress orientation. As discussed in Section 3.2.1, the effects of the wellbore deviation and the stress orientation are closely linked. For example, Figure 18 indicates that with wellbore rotation about σ_v only, the cases under the reverse or strike-slip condition consistently produce longitudinal and planar fractures, whereas those under the normal stress condition lead to inclined and curved fractures. However, the observation becomes different when the wellbore rotation axis changes to σ_H: the normal stress condition results in longitudinal and planar fractures instead, while the fractures formed in the strike-slip cases become inclined and curved. This is due to the fact that, in the normal stress regime, σ_v is larger than σ_H, so the near-well fracture tends to grow in the direction that is normal to the σ_H direction. When the wellbore deviates about σ_H, its axis remains perpendicular to σ_H as the no-deviation case, thus fractures are still planar and longitudinal. However, when deviated around σ_v, the wellbore gets oblique to σ_H, thereby causing fractures to incline and curve. In contrast, the strike-slip cases have $\sigma_H > \sigma_v$, therefore the behavior becomes exactly the opposite. This also explains why the normal and strike-slip cases both produce inclined and curved fractures when the well is rotated about both σ_v and σ_H axes. As for the reverse stress condition, the near-well fractures are commonly less inclined and curved compare with the cases under other two stress orientations. It is because in the reverse stress regime where $\sigma_H > \sigma_h > \sigma_v$, the difference between σ_H and σ_v is maximized, leading to the near-well fracture is mostly controlled by the in situ stress direction. On the contrary, the stress difference becomes

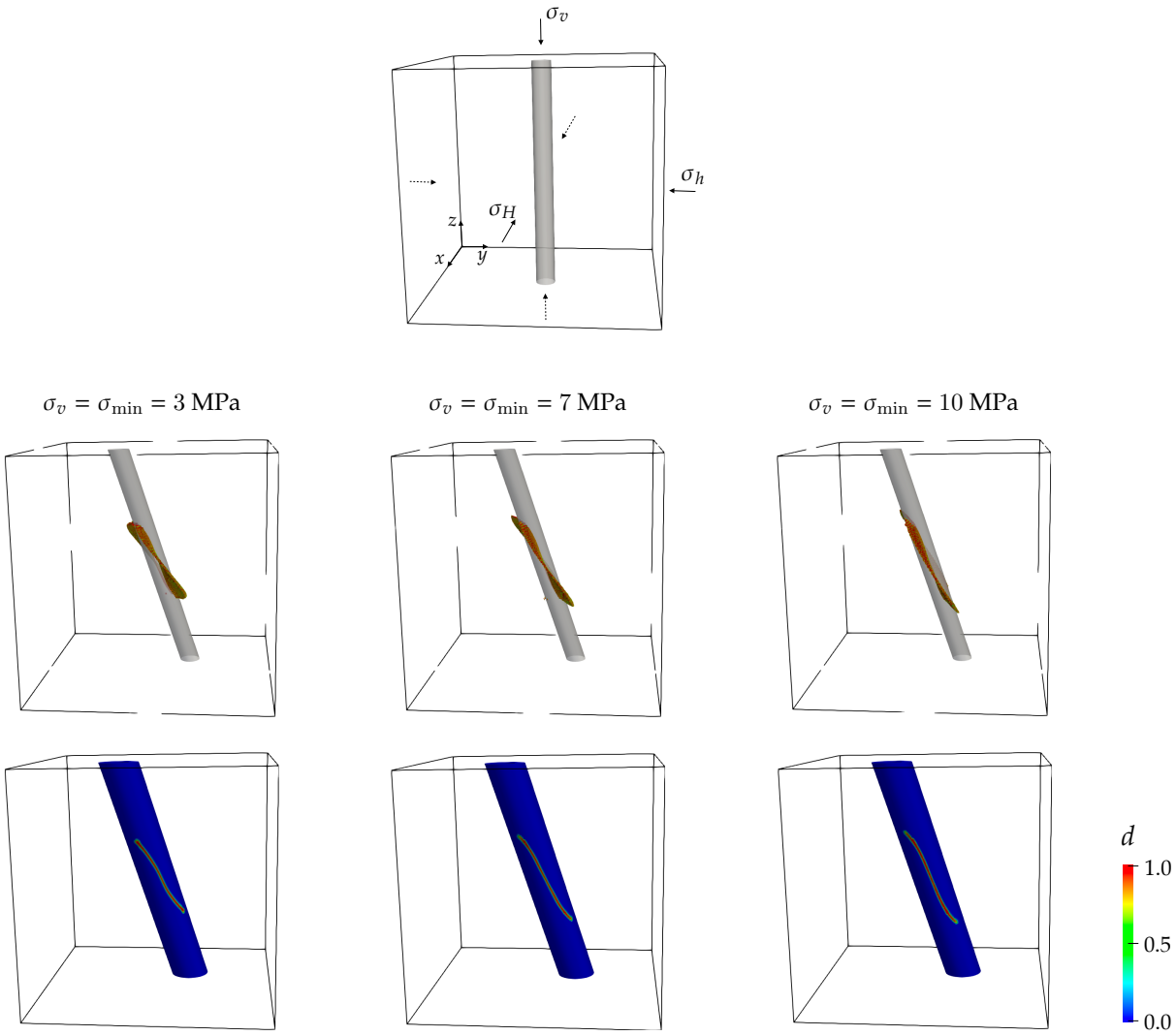

Figure 16: Vertical well: near-well fracture results for representative examples under varying stress magnitudes.

much smaller in the normal and strike-slip cases, making near-well fractures more sensitive to wellbore deviation. The similar trend can be observed in fracture azimuths as presented in Tables 7-9: in the reverse stress regime, the fracture nucleation consistently shows less deviation from its original position in the no-deviation case compared to the other two stress regimes.

Regarding the magnitude of $\sigma_{\min}$, its overall effects are analogous to what we observed in the vertical well case: an increasing stress magnitude lowers the fracture inclination and curvature, making the results more stress-controlled. For example, as indicated in Figure 17 where the wellbore is rotated about σ_v, the cases under the normal stress condition yield less inclined fractures as $\sigma_{\min}$ (σ_h) increases. The reverse stress cases also manifest the same effect, as shown in Figures 18 & 19, that the near-well fractures are mostly inclined at a lower $\sigma_{\min}$ (σ_v), while they become more aligned with the well when $\sigma_{\min}$ increases. In addition to the fracture geometry and alignment, the fracture azimuth experiences similar effects by the stress magnitude. With rotation about both σ_v and σ_H axes, the normal stresss cases (Table 7 and strike-slip cases (Table 9) generally exhibit a more deviated fracture nucleation position at a smaller value of σ_{min} (σ_h). As for the reverse stress condition, the influence of the stress magnitude on the fracture azimuth is unclear, probably for the same reason we identified for vertical well cases in the normal stress regime: an increasing σ_{min} (σ_v) reduces the difference between σ_H and σ_v, thereby diminishing the effects of the stress magnitude.

3.3 Comparison with the experimental observations

Let us now compare the simulation results with the experimental observations from Task 4 to assess whether the model replicates the trends observed in laboratory tests. Figure 20 displays the experimental results for both vertical and horizontal wells, excluding those under thermal treatment (i.e., pre-circulation). In these tests, all wells are subject to normal stress conditions (i.e., $\sigma_v > \sigma_H > \sigma_h$), with σ_v and σ_H held constant at 17.5 MPa and 15 MPa, respectively. For the vertical well, all cases at σ_h = 10 MPa exhibit longitudinal near-well fractures, consistent with the numerical results in Figure 3, which show no fracture inclination when the well is non-deviated. Even when the well is deviated in the simulation, the fracture inclination remains minimal at σ_h = 10 MPa. However, in the horizontal well, inclined fractures are observed. This could be attributed to slight wellbore deviation during sample preparation, potential shear stress at the boundaries, or material heterogeneities. Notably, the results indicate that the fracture inclination increases as σ_h decreases. This aligns well with the trend observed in the numerical tests, as shown in Figure 9, that the fracture becomes more inclined at lower $\sigma_{\min}$ (σ_h in this case).

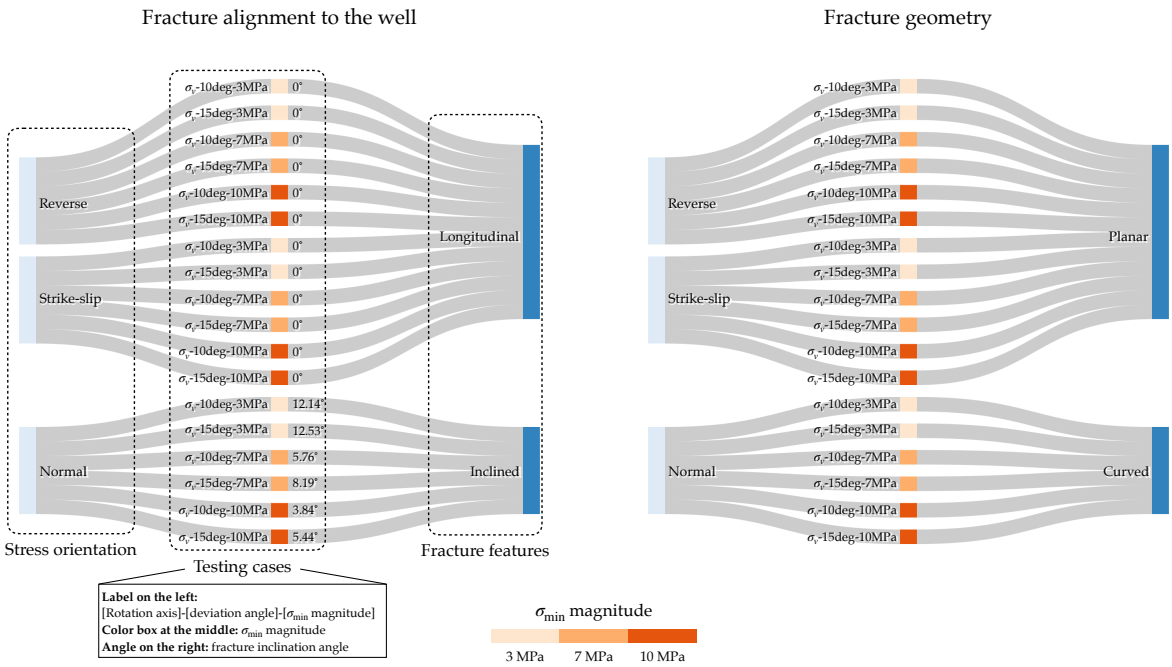

Figure 17: Horizontal well: summary of simulation results for different stress conditions with well rotation about σ_v axis, focusing on the fracture alignment (left) and geometry (right). The left column shows the stress regime. The middle column consists of the case label, a color box indicating σ_{min} magnitude, and the fracture inclination angle if applicable. The right column shows the fracture feature, where "Mixed" indicates an intermediate state.

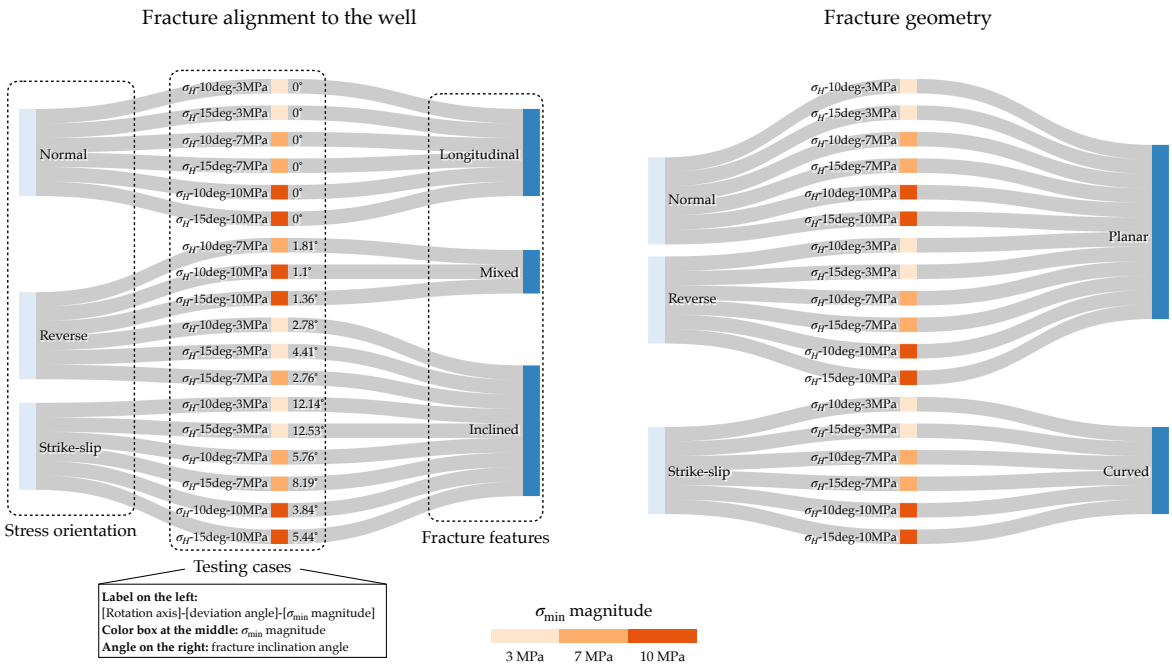

Figure 18: Horizontal well: summary of simulation results for different stress conditions with well rotation about σ_H axis, focusing on the fracture alignment (left) and geometry (right). The left column shows the stress regime. The middle column consists of the case label, a color box indicating σ_{min} magnitude, and the fracture inclination angle if applicable. The right column shows the fracture feature, where "Mixed" indicates an intermediate state.

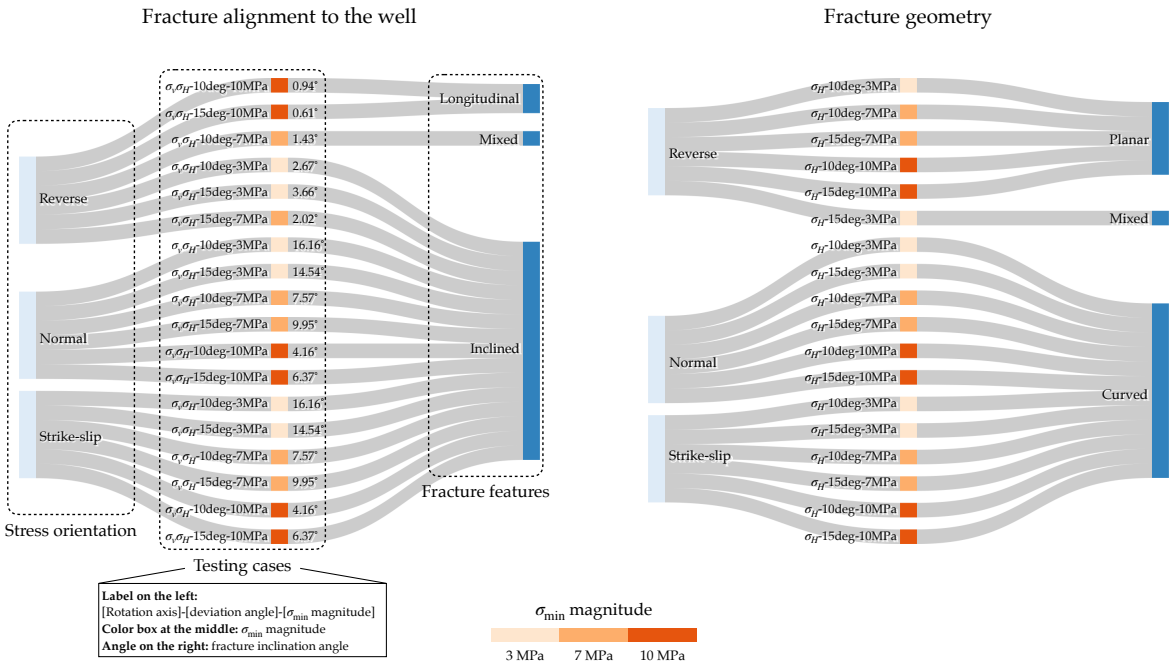

Figure 19: Horizontal well: summary of simulation results for different stress conditions with well rotation about both σ_v & σ_H axes, focusing on the fracture alignment (left) and geometry (right). The left column shows the stress regime. The middle column consists of the case label, a color box indicating σ_{min} magnitude, and the fracture inclination angle if applicable. The right column shows the fracture feature, where "Mixed" indicates an intermediate state.

1) Vertical well-Room temperature sample-Non-Thermal Stress (VR-NTS)
2) Vertical well-High temperature sample-Non-Thermal Stress (VH-NTS)
3) Vertical well-High temperature sample-Induced Thermal Stress (VH-ITS)
4) Horizonal well-High temperature sample-Induced Thermal Stress (HH-ITS)
5) Horizonal well-Room temperature sample-Non-Thermal Stress (HR-NTS)

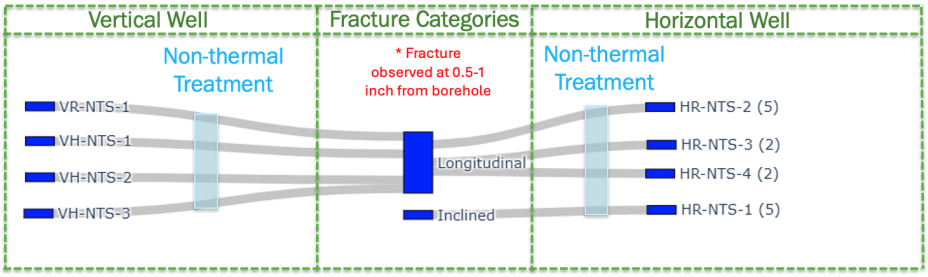

Longitudinal: fracture parallel to wellbore drilling direction
Inclined: Fracture angles with wellbore drilling direction range from 10 to 45 degrees.

Figure 20: Classification of fracture patterns from experimental results. All wells are subjected to the normal stress condition with σ_v = 17.5 MPa and σ_H = 15 MPa. For vertical wells, σ_h is 10 MPa. For horizontal wells, σ_h varies according to the ratio indicated in the parentheses.

4 Conclusions & Future Work

Using a novel phase field formulation capable of capturing both hydraulic fracture nucleation in the bulk rock material and fracture propagation, we have presented a comprehensive numerical investigation of the impact of in situ stress conditions and wellbore orientation on fracture nucleation patterns in granite. Model parameters were calibrated based on experimental results conducted as part of the same research project.

Future work will focus on two main directions to extend the current study. First, the model will be applied to interpret fracturing tests conducted at the FORGE site. By simulating minifrac tests and using image logs as input data, the model will be employed to invert for in situ stress conditions.

Second, thermal effects will be incorporated into the model, as experimental evidence from this project has shown that thermal stresses significantly influence fracture nucleation patterns. Developing a model that accounts for these effects will not only enhance the understanding of thermo-mechanical interactions but also provide a unique framework for explaining some of the observed experimental results.

Third, the current numerical simulations assume a homogeneous domain without initial damage or defects. In real-world scenarios, heterogeneities and pre-existing defects are common and can have a significant impact on near-well fracture nucleation and propagation. Future studies could incorporate these complexities to provide a more comprehensive and realistic analysis of near-well fracture behavior.

Data availability

All numerical simulations were performed using the open-source GEOS simulation framework (Settgast et al., 2024) and simulation decks are available at https://github.com/GEOS-DEV/FORGE.

References

Fei, F., Costa, A., Dolbow, J. E., Settgast, R. R., & Cusini, M. (2023). A phase-field model for hydraulic fracture nucleation and propagation in porous media. *International Journal for Numerical and Analytical Methods in Geomechanics*, *47*(16), 3065-3089. Retrieved from `https://onlinelibrary.wiley.com/doi/abs/10.1002/nag.3612` doi: https://doi.org/10.1002/nag.3612

Kumar, A., Bourdin, B., Francfort, G. A., & Lopez-Pamies, O. (2020). Revisiting nucleation in the phase-field approach to brittle fracture. *Journal of the Mechanics and Physics of Solids*, *142*, 104027.

Lu, Y. (2017). *Laboratory studies on thermal fracturing behavior in well stimulation of enhanced geothermal systems* (Unpublished doctoral dissertation).

Miehe, C., & Mauthe, S. (2016). Phase field modeling of fracture in multi-physics problems. part iii. crack driving forces in hydro-poro-elasticity and hydraulic fracturing of fluid-saturated porous media. *Computer Methods in Applied Mechanics and Engineering*, *304*, 619–655.

Mikelić, A., Wheeler, M. F., & Wick, T. (2015). Phase-field modeling of a fluid-driven fracture in a poroelastic medium. *Computational Geosciences*, *19*(6), 1171–1195.

Pijaudier-Cabot, G., Dufour, F., & Choinska, M. (2009). Permeability due to the increase of damage in concrete: From diffuse to localized damage distributions. *Journal of engineering mechanics*, *135*(9), 1022–1028.

Settgast, R. R., Aronson, R. M., Besset, J. R., Borio, A., Bui, Q. M., Byer, T. J., ... Wu, H. (2024). Geos: A performance portable multi-physics simulation framework for subsurface applications. *Journal of Open Source Software*, *9*(102), 6973. Retrieved from `https://doi.org/10.21105/joss.06973` doi: 10.21105/joss.06973

Yu, W., Bao-lin, L., Hai-yan, Z., Chuan-liang, Y., Zhi-jun, L., & Zhi-qiao, W. (2014). Thermophysical and mechanical properties of granite and its effects on borehole stability in high temperature and three-dimensional stress. *The Scientific World Journal*, *2014*(1), 650683.

Zoback, M. D. (2010). *Reservoir geomechanics*. Cambridge university press.